



# Photocatalytic degradation of atrazine by boron-doped TiO<sub>2</sub> with a tunable rutile/anatase ratio



Wei-Kang Wang<sup>1</sup>, Jie-Jie Chen<sup>1</sup>, Miao Gao, Yu-Xi Huang, Xing Zhang\*, Han-Qing Yu\*

CAS Key Laboratory of Urban Pollutant Conversion, Department of Chemistry, University of Science & Technology of China, Hefei, 230026, China

## ARTICLE INFO

### Article history:

Received 11 February 2016

Received in revised form 19 April 2016

Accepted 4 May 2016

Available online 7 May 2016

### Keywords:

Atrazine

B-doped TiO<sub>2</sub>

Phase-junction

Photocatalytic degradation

Tunable ratio

## ABSTRACT

Atrazine is a widely used herbicide and a typical toxic pollutant. TiO<sub>2</sub>-mediated photocatalysis is an efficient way to degrade such a refractory contaminate. In a photocatalytic process, great charge separation and efficient interparticle electron transfer are highly desired and are usually achieved through element doping and phase-junction optimization. However, in the traditional methods for synthesizing phase-junction TiO<sub>2</sub>, high phase transition temperature and appropriate adjusters are always needed. In this work, boron-doped (B-doped) TiO<sub>2</sub> with a tunable anatase/rutile ratio is successfully synthesized for efficient atrazine degradation by using a simple one-step calcination method, which is conducted below phase transition temperature with as-prepared Ti and B mixture as a precursor. The formation of the surface-phase junctions between anatase and rutile nanoparticles enables effective interparticle electron transfer and results in more efficient charge separation. Also, the B-doping serves as charge traps, which are able to mediate oxidative electron transfer. The prepared B-doped TiO<sub>2</sub> exhibits a higher photocatalytic activity for the degradation of atrazine, with a reaction rate of 4 times faster than that of the non-doped counterpart. The photogenerated reactive species and degradation intermediates of atrazine are identified, and the photocatalytic atrazine degradation mechanism is elucidated. This study provides a new approach to prepare phase-junction photocatalysts and demonstrates that the anatase/rutile ratio can be tuned by doping element. Such a “killing two birds with one arrow” strategy could be extended for preparing other photocatalysts for the degradation of various pollutants.

© 2016 Elsevier B.V. All rights reserved.

## 1. Introduction

Atrazine, a widely used herbicide, has attracted interests because of its wide use in agriculture, high toxicity and slow biodegradation in the environment [1]. Many techniques have been developed to treat atrazine-contaminated water, including microbiological process [2,3], electrochemical method [4–6], photocatalysis [7,8], etc. Among them, photocatalysis has given much attention in view of its facility, efficiency, cost effectiveness, and utilization of solar energy.

TiO<sub>2</sub> is an intriguing semiconductor photocatalyst because of its chemical inertness, photostability, and environmentally friendly features. However, undesired recombination of photoexcited carriers and wide band gap (3.2 eV) severely limits its practical application. Doping with other elements, as a simple and feasible

approach, has been widely used for TiO<sub>2</sub> modification to improve its photocatalytic activity [9]. In particular, doping of nonmetals seems to be an effective way [10]. Also, it is a promising way to achieve visible light activity of TiO<sub>2</sub> via nonmetal element doping, such as N, C, S, P, and halogen atoms. Among them, boron doping has been adopted in electrochemical studies, because it can enhance the electron-accepting capacity of TiO<sub>2</sub> [11]. Boron atom tends to either replace an oxygen atom or sits in the interstitial position. Furthermore, density functional calculations about the electronic structure of the B-doped reveal that the *p* orbital of B is mixed with O 2*p* orbitals, which is responsible for the band gap narrowing [12].

At the same time, phase-junction TiO<sub>2</sub> has received extensive interests to improve the photocatalytic activity of TiO<sub>2</sub> because phase-junction can be advantageous to the separation of photogenerated electron-hole pairs, thus prolonging the recombination time [13]. Our previous work has demonstrated that the phase-junction TiO<sub>2</sub> with a relatively small fraction of rutile content has a favorable photocatalytic activity for pollutant degradation [14].

As shown in a previous study [15], more Cl and/or H<sub>2</sub>O could shield positive charges at a relatively high HCl/Ti ratio and serve to lessen the effects of electrostatic stabilization (repulsion) to

\* Corresponding authors.

E-mail addresses: [zhx0610@ustc.edu.cn](mailto:zhx0610@ustc.edu.cn) (X. Zhang), [hqyu@ustc.edu.cn](mailto:hqyu@ustc.edu.cn) (H.-Q. Yu).

<sup>1</sup> These authors contributed equally.

optimize the phase-junction  $\text{TiO}_2$  formation in annealing process. Furthermore,  $\text{H}_3\text{BO}_3$ , which was used as the source of boron added into the synthesis process of phase-junction  $\text{TiO}_2$  nanocrystals, might have the same effect as  $\text{HCl}$  to tune the phase ratio and simultaneously achieve B doping. The currently available routes to synthesize phase-junction  $\text{TiO}_2$  need organic reagents, complex processes and templates [16,17]. It is therefore highly desirable to develop a simple method, which can optimize the doping content and achieve a reasonable anatase/rutile (A/R) ratio to improve the photocatalytic performance.

Herein, B-doped  $\text{TiO}_2$  (A/R) nanoparticles were successfully synthesized with  $\text{H}_3\text{BO}_3$  and  $\text{Ti}^{3+}$  solution by a one-step annealing method below phase-transition temperature. Two strategies in synergy were adopted to improve the photocatalytic performance of  $\text{TiO}_2$  nanoparticles. Systematical characterization was carried out to explore the influence of B doping on the electronic band structures, optical properties, separation and transfer of photo-generated electron-hole pairs in  $\text{TiO}_2$  (A/R), and the generation of reactive oxygen species in photocatalysis. Also, the capacity of the as-prepared B-doped  $\text{TiO}_2$  (A/R) as a photocatalyst for the degradation of atrazine under irradiation was evaluated. Furthermore, a plausible mechanism for the photocatalytic atrazine degradation in the B-doped  $\text{TiO}_2$  (A/R) and the photocatalytic degradation pathways were elucidated.

## 2. Materials and methods

### 2.1. Synthesis of B-doped $\text{TiO}_2$ (A/R) nanocomposites

All chemicals used in this work were analytical-grade reagents and used without further purification.

The B-doped  $\text{TiO}_2$  (A/R) nanocomposites were prepared as follows: a 0.30 mm thick Ti foil (0.6 g Ti) was cleaned with acetone, alcohol and deionized water sequentially, and then added into Teflon-lined stainless autoclaves with 50 mL of effective volume. Then, a mixture of water (20 mL) and concentrated hydrochloric acid (20 mL) was slowly added into the autoclave. After that, the sample was autoclaved at  $160^\circ\text{C}$  for 2 h and then naturally cooled under room temperature to obtain solution [18]. Later,  $\text{H}_3\text{BO}_3$  of different dosage (0, 15, 30, 60, 120, and 150 mg) was dispersed into 10 mL of as-prepared solution. The as-prepared solutions with different amounts of  $\text{H}_3\text{BO}_3$  were annealed at  $500^\circ\text{C}$  for 2 h with a heating rate of  $5^\circ\text{C}/\text{min}$  in air. The obtained products using

different amounts of  $\text{H}_3\text{BO}_3$  were denoted as B1, B2, B3, B4, B5, and B6.

### 2.2. Characterization of the photocatalysts

The Power X-ray diffraction (XRD) patterns were obtained by a Rigaku diffractometer (TTR-III, Rigaku Co., Japan), using  $\text{Cu K}\alpha$  radiation source ( $\lambda = 1.541841 \text{ \AA}$ ) at a scan speed of  $8^\circ/\text{min}$  to determine the crystal phase of the obtained samples with an accelerating voltage and current of 40 kV and 200 mA, respectively. The morphology and structure of the samples were characterized by a transmission electron microscopy (TEM) (JEM2100, JEOL Inc., Japan). The high-resolution transmission electron microscopy (HRTEM) images were taken on an HRTEM (JEM-2010, JEOL Inc., Japan) at an acceleration voltage of 200 kV. The diffuse reflectance spectra (DRS) of the samples were measured on a UV-vis spectrophotometer (SOLID3700, Shimadzu Co., Japan). The chemical composition was characterized by X-ray photoelectron spectroscopy (PHI 5600 XPS spectroscopy, Ulvac-Phi Co., Japan). Fourier transform infrared spectra (FTIR) were recorded on a Vertex 70 spectrometer (Bruker Co., Germany) under the transmission scheme by using the KBr pellet technique.

### 2.3. Photocatalytic degradation of atrazine

The photocatalytic degradation of atrazine by all the B-doped  $\text{TiO}_2$  samples was performed. 20 mg of non-doped and doped  $\text{TiO}_2$  nanoparticles were dispersed in 40-mL atrazine solution (10 mg/L) and stirred in dark for 30 min to establish adsorption-desorption equilibrium between the solution and the catalysts. Later, for the photocatalytic reaction, each pollutant solution was irradiated using a 350 W (15 A) Xenon lamp with a 300 nm cutoff filter (CHF-XM-350W, Beijing Trustech. Co., China) as the light source. The photocatalytic tests were conducted in a 50-mL beaker with a cold bath. After given time intervals, 1 mL of aqueous solution was filtered out from the reactor vessel.

The atrazine concentration was measured by high-performance liquid chromatography (HPLC-1100, Agilent Inc., USA) with a Hypersil-ODS reversed-phase column and detected at 254 nm using a VWD detector. The mobile phase was a mixture of water and methanol (40:60) delivered at a flow rate of  $0.8 \text{ mL min}^{-1}$ . The atrazine degradation intermediates were analyzed by liquid chromatography mass spectrometry (LC/MS, 6460, Agilent Inc., USA).

Since  $\cdot\text{OH}$  can react with terephthalic acid (TA) to generate 2-hydroxy terephthalic acid (TAOH), which emits unique

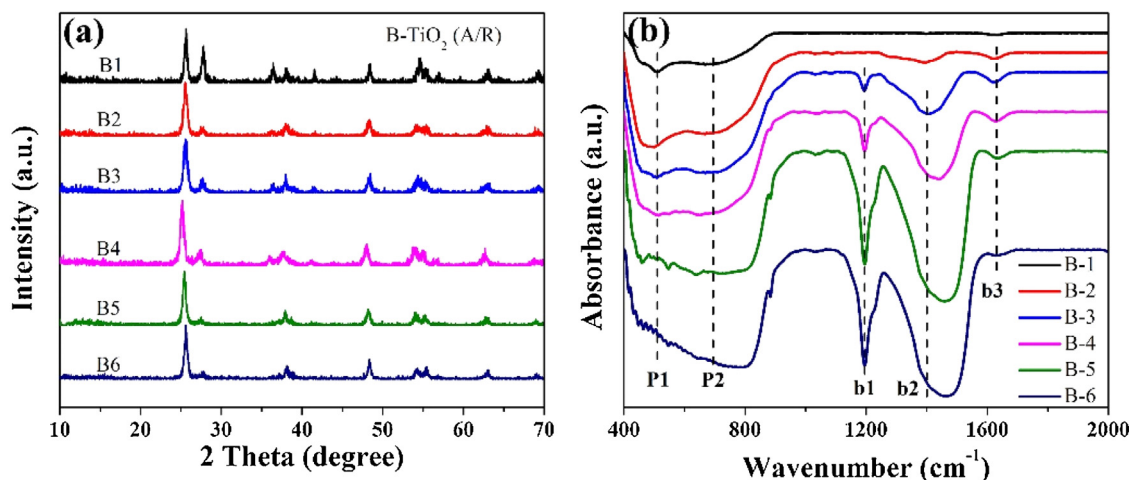


**Fig. 1.** (a) XRD patterns and (b) FTIR spectra of the B-doped  $\text{TiO}_2$  (A/R) nanoparticles with different B doping contents: 0 mg (B1), 15 mg (B2), 30 mg (B3), 60 mg (B4), 120 mg (B5), and 150 mg (B6).

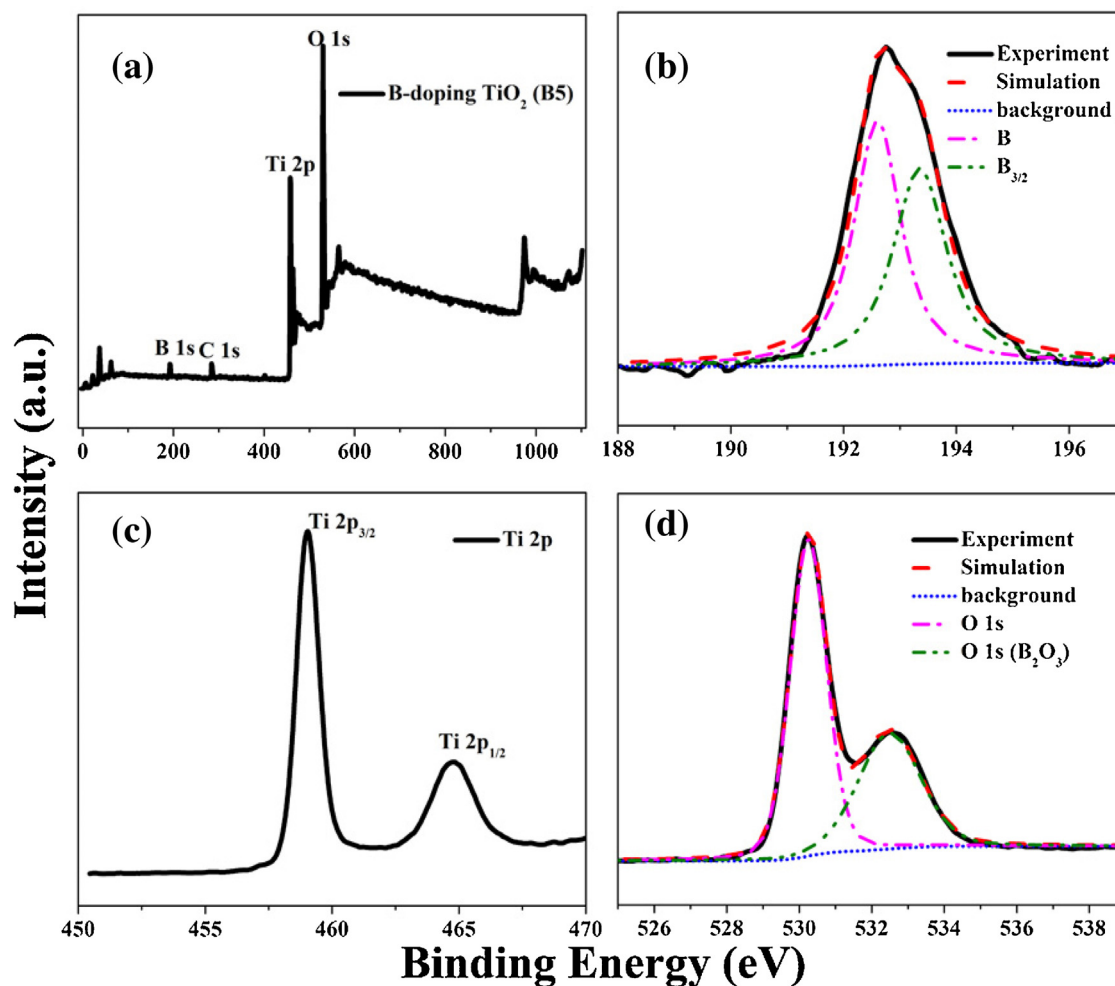


Fig. 2. XPS spectra of the B-doped  $\text{TiO}_2$  (A/R) sample (B5): (a) Survey spectra, (b) B 1s, (c) Ti 2p, and (d) O 1s.

fluorescence at 426 nm [19], significant fluorescent signals associated with TAOH are generated upon the UV–vis light irradiation of the samples suspended in 3 mM TA solution containing 10 mM NaOH for different irradiation times. The hydroxyl radical ( $\bullet\text{OH}$ ) concentration was detected at room temperature by Fluorescence spectrometer (LS 55, Perkin Elmer Inc., USA) with 310 nm as the excitation number.

### 3. Results and discussion

#### 3.1. Structural and chemical characteristics of the $\text{TiO}_2$ (A/R) nanocomposites

Fig. 1a shows the XRD patterns of the samples with different B doping contents. The crystallized structures for the non-doped and doped samples mainly consist of anatase phase (corresponding to  $2\theta = 25.4^\circ$ ) and rutile phase (corresponding to  $2\theta = 27.5^\circ$ ). This shows that two phases of anatase and rutile were present in the  $\text{TiO}_2$  nanocomposites. The phase contents of the samples can be estimated from the XRD peak intensities with the following equations [20]:

$$f_A = \frac{1}{1 + \frac{1}{K} \frac{I_R}{I_A}} \quad (1)$$

$K = 0.79$ , if  $f_A > 0.2$ ;

$K = 0.68$ , if  $f_A \leq 0.2$ .

where  $f_A$  is the fraction of anatase phase in the powder, and  $I_A$  and  $I_R$  are the X-ray intensities of the anatase (101) and rutile (110) diffraction peak, respectively. The weight percentages of rutile in the six samples were estimated to be 51.8, 12.6, 20.9, 17.5, 10.3 and 7.5 wt%, respectively. Furthermore, compared with the non-doped, the XRD pattern shows that the rutile content of the samples B2–B6 decreased and the main peak locations of anatase and rutile appeared to shift to a certain degree with B doping.

Our previous studies have demonstrated that a relatively high HCl/Ti ratio in the solution could lessen the effects of electrostatic repulsion, which would be hazardous to the formation of rutile [14,21]. In addition, the presence of  $\text{H}_3\text{BO}_3$  introduced electrostatic attraction, further promoting the formation of anatase phase. Therefore, the  $\text{TiO}_2$  phases are tuned by the synergistic effects of HCl and  $\text{H}_3\text{BO}_3$ .

The FTIR spectra of the B-doped  $\text{TiO}_2$  (Fig. 1b) could be validated by the IR finger band below  $1000\text{ cm}^{-1}$ , characteristic of the Ti–O–Ti network, and the three intense signals at 1190, 1400, and  $1620\text{ cm}^{-1}$ . There is an obvious evolution from two peaks at 694 and  $500\text{ cm}^{-1}$  to a single peak at  $690\text{ cm}^{-1}$ , as indicated by P1 and P2. To understand the origin of the two peaks, the IR spectra of the two-phase mixed  $\text{TiO}_2$  was examined. The referenced anatase  $\text{TiO}_2$  has one peak at  $694\text{ cm}^{-1}$ , and the rutile  $\text{TiO}_2$  has two peaks at 656 and  $528\text{ cm}^{-1}$ . Thus, the peak at  $525\text{ cm}^{-1}$  of the samples in Fig. 1b was

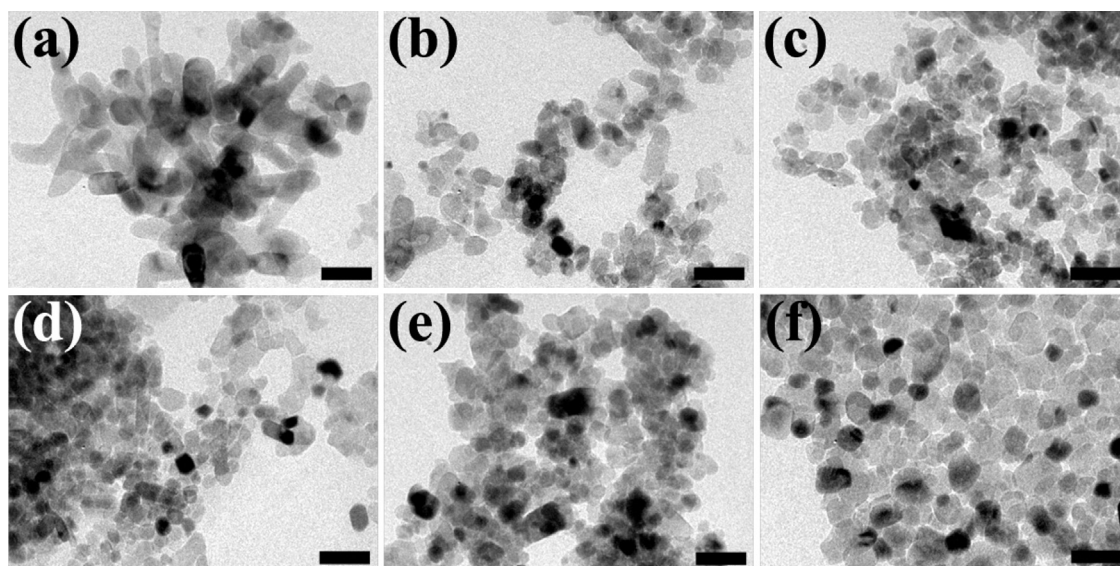


Fig. 3. Typical TEM images of the B-doped TiO<sub>2</sub> (A/R) sample: (a) B1, (b) B2, (c) B3, (d) B4, (e) B5, and (f) B6. Scale bar: 60 nm.

from rutile TiO<sub>2</sub> and the gradually predominant peak at 664 cm<sup>-1</sup> was attributed to the integrated anatase and rutile structure [22].

Apart from 1000 cm<sup>-1</sup> below, the three intense signals at 1190, 1400, and 1620 cm<sup>-1</sup> were observed. The vibrational band at 1620 cm<sup>-1</sup> may be unambiguously assigned to the surface-adsorbed water and hydroxyl groups (denoted as b3). The band at 1400 cm<sup>-1</sup> might be ascribed to the presence of tri-coordinated (in the form of B 3p) interstitial boron (denoted as b2), which tends to interact with ambient oxygen atoms to exhibit chemical environments similar to that of normal Ti-O-B, whereas the band at 1190 cm<sup>-1</sup> should be attributed to the stretching vibrations of the B-O bonds (denoted as b1) [23]. Such an observation is in good agreement with the XRD results. Briefly, the afore-discussed FTIR results reveal that the boron species in the B-doped TiO<sub>2</sub> mainly were present as trico-ordinated interstitial B and 'boroxol rings'. Nevertheless, the existence of oxygen-substituted B could not be ruled out.

In addition to the FTIR spectra analysis, XPS was also used to explore the chemical state of the dopant species incorporated into the TiO<sub>2</sub> lattice. The core level energies of B 1s, O 1s, and Ti 2p of the sample B5 are shown in Fig. 2a. The B 1s XPS spectrum could be used to identify the boron species on the surface of the doped TiO<sub>2</sub>. As shown in Fig. 2b, the B 1s XPS spectrum of the B-doped TiO<sub>2</sub> exhibited the typical asymmetrical broad peak in the range of 191.0–195.0 eV, which might be deconvoluted (carried out by the XPS PEAK41 software package) into two overlapped peaks centered at 192.6 and 193.3 eV. The former peak at 192.6 eV could be ascribed to interstitial boron, and the peak at 193.3 eV should be attributed to signal originated from BO<sub>3/2</sub> polymer and/or surface BO<sub>3/2</sub> species [12,23]. Similar assignments could also be made for the B from the FTIR spectra analysis. Furthermore, compared with BO<sub>3/2</sub> species, spectral analyses revealed that the concentrations of the interstitial boron amount to more of the total boron B-doped TiO<sub>2</sub> in agreement with FTIR spectra analysis.

Furthermore, the Ti 2p<sub>3/2</sub> XPS spectrum of the B-doped TiO<sub>2</sub> exhibited a peak responsible for at 459.0 eV, in addition to the 2p<sub>1/2</sub> peak at 464.7 eV (Fig. 2c). Moreover, the O 1s (B<sub>2</sub>O<sub>3</sub>) (Fig. 2d) had a peak responsible for BO<sub>3/2</sub> species from the B XPS spectrum.

Fig. 3 shows the low magnification TEM images of the B-doped TiO<sub>2</sub> samples fabricated at different H<sub>3</sub>BO<sub>3</sub> concentrations. The controlled nanocomposite (B1) had many nanorods. With increasing B-doped content, the obtained samples had many nanoparticles

along with occasional nanorods. All these samples show similar morphologies, i.e., aggregates of TiO<sub>2</sub> nanoparticles and nanorods with different sizes.

In order to provide direct evidence to support the existence of anatase and rutile phases, the synthesized B-doped TiO<sub>2</sub> samples were further subjected to HRTEM analysis. Fig. 4 shows the HRTEM images of B5. The lattice spacing of 0.32 nm, which corresponds to the (110) plane of the rutile lattice, was clearly observed. In addition, the lattice spacing of neighbor nanoparticle was 0.35 nm, which corresponds to the (101) plane of the anatase lattice. Therefore, the HRTEM results further confirm the co-existence of the rutile and anatase phases in the TiO<sub>2</sub> nanocomposites. Moreover, the phase-junction between rutile and anatase nanoparticles could be clearly seen from the HRTEM image.

### 3.2. Photophysical properties of the TiO<sub>2</sub> (A/R) nanocomposites

The optical absorption properties of semiconductor materials are associated strongly with their electronic band structures. The effects of boron doping on the light absorption characteristics of TiO<sub>2</sub> nanoparticles are shown in Fig. 5. The insert chart in Fig. 5 is

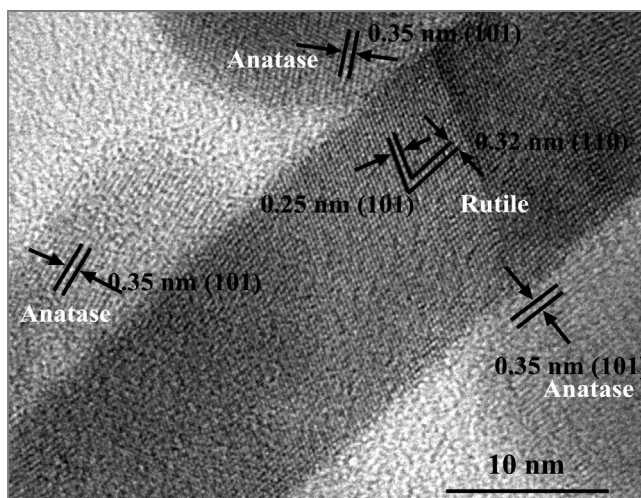


Fig. 4. HRTEM image of the B-doped TiO<sub>2</sub> (A/R) sample (B5).

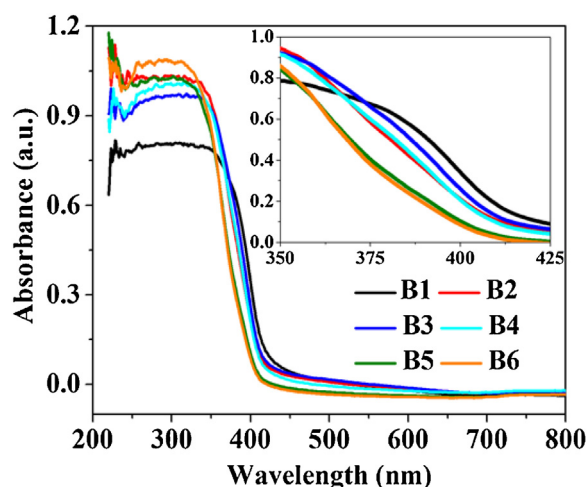


Fig. 5. UV-vis diffuse reflection spectra of all the TiO<sub>2</sub> (A/R) samples.

the enlarged figure at 350–425 nm. The absorption edge position of all B-doped TiO<sub>2</sub> exhibited a large blue shift, implying that the band gap of B-doped TiO<sub>2</sub> increased because of the much larger band gap of BO<sub>x</sub> than TiO<sub>2</sub>. This is because the doped boron ion was situated in the interstitial TiO<sub>2</sub> structure, forming a possible chemical environment such as Ti–O–B [24,25]. On the other hand, a blue-shift of UV-vis absorption edge might be caused due to the reduction of the rutile content by doping [26]. Thus, the B-doped TiO<sub>2</sub> absorbance was attributed to the coupling effects of the rutile and boron contents. This could be used to explain why B2 had a more blue shift compared with B3 and B4. In addition, compared with non-doped TiO<sub>2</sub>, the optical absorption intensity of the B-doped TiO<sub>2</sub> nanocomposites was enhanced [27]. This resulted in their improved photocatalytic activity in the UV-vis region.

### 3.3. Photocatalytic atrazine degradation performance

To evaluate the photoactivity of the B-doped TiO<sub>2</sub> samples, photocatalytic experiments for the degradation of atrazine were

Table 1

Efficiencies and rate constants ( $k$ ) of atrazine degradation by the catalysts prepared at H<sub>3</sub>BO<sub>3</sub> concentrations.

Catalyst	Rutile content (wt%)	Degradation efficiency (%)	$k$ (min <sup>-1</sup> )	H <sub>3</sub> BO <sub>3</sub> dosage (mg)
B1	51.8	50.0	−0.0038	0
B2	12.6	81.1	−0.0086	15
B3	20.9	77.5	−0.0070	30
B4	17.5	76.6	−0.0073	60
B5	10.3	95.0	−0.0160	120
B6	7.5	78.0	−0.0082	150

conducted (Fig. 6). The blank control (without photocatalyst) showed a stable concentration of atrazine under UV-vis light irradiation. The presence of the B-doped TiO<sub>2</sub> samples resulted in a rapid decrease in atrazine concentration, and the highest atrazine degradation efficiency (94.7%) was achieved by B5 during 180-min light irradiation. The non-doped TiO<sub>2</sub> samples showed the total atrazine photodegradation of only 50.1%. For all samples, the photodegradation of atrazine increased substantially with the decreasing rutile amount to 11.6 wt%. This result suggests that the rutile-anatase ratio plays a vital role in governing the recombination of photo-generated h<sup>+</sup>/e<sup>−</sup> pairs for the two-phase mixed TiO<sub>2</sub>, and affecting its photocatalytic activity (Table 1).

The atrazine photodegradation process over time by B5 in Fig. 6c shows that the intermediates (retention time of 3–6 min) began to accumulate, and then declined owing to the greater degradation rate than the accumulation one. Fig. 6b illustrates the atrazine photodegradation process over time, which follows the pseudo-first-order kinetics owing to the intermediates degradation process [28]. Therefore, the apparent degradation rate constant ( $k$ ) of atrazine could be calculated from the slope of the  $\ln(C/C_0)$  versus time fitting line, in which  $C$  represents the atrazine concentration. A comparison of the atrazine degradation rate constants with different photocatalysts reveals that the fastest atrazine degradation was achieved by the two-phase mixed TiO<sub>2</sub>. In addition,  $k_{B5}$  was larger than the others in absolute value, suggesting that the optimal B-doped content in the phase-junction TiO<sub>2</sub> was favorable for enhancing the photocatalytic degradation capability.

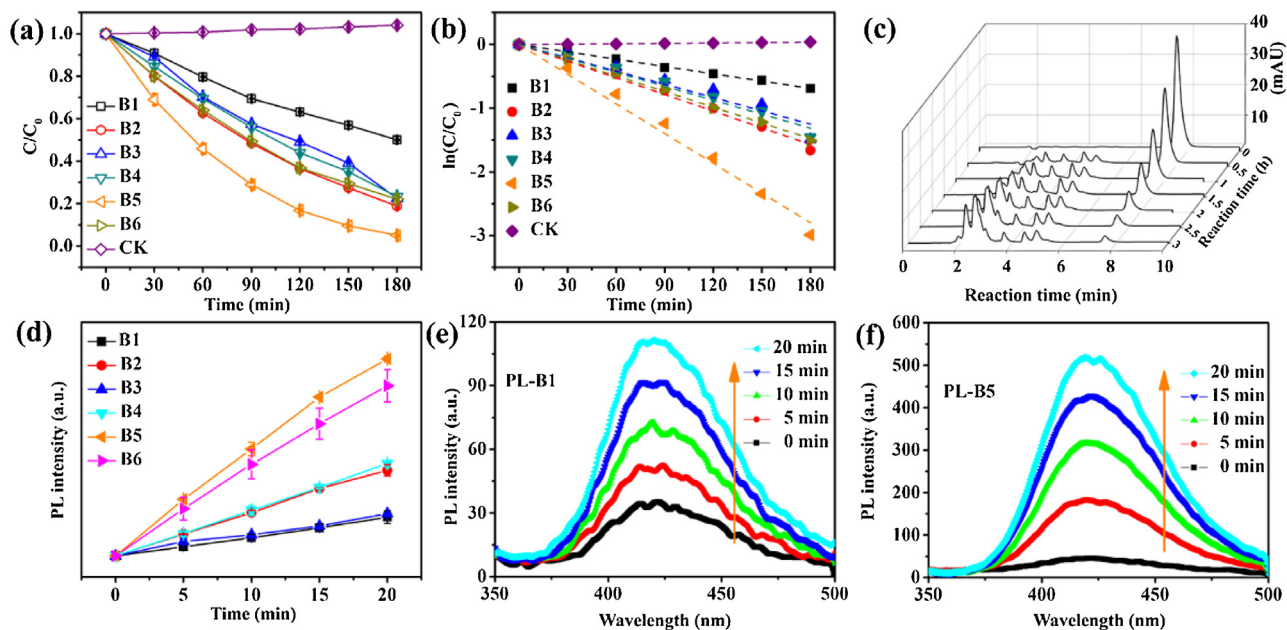
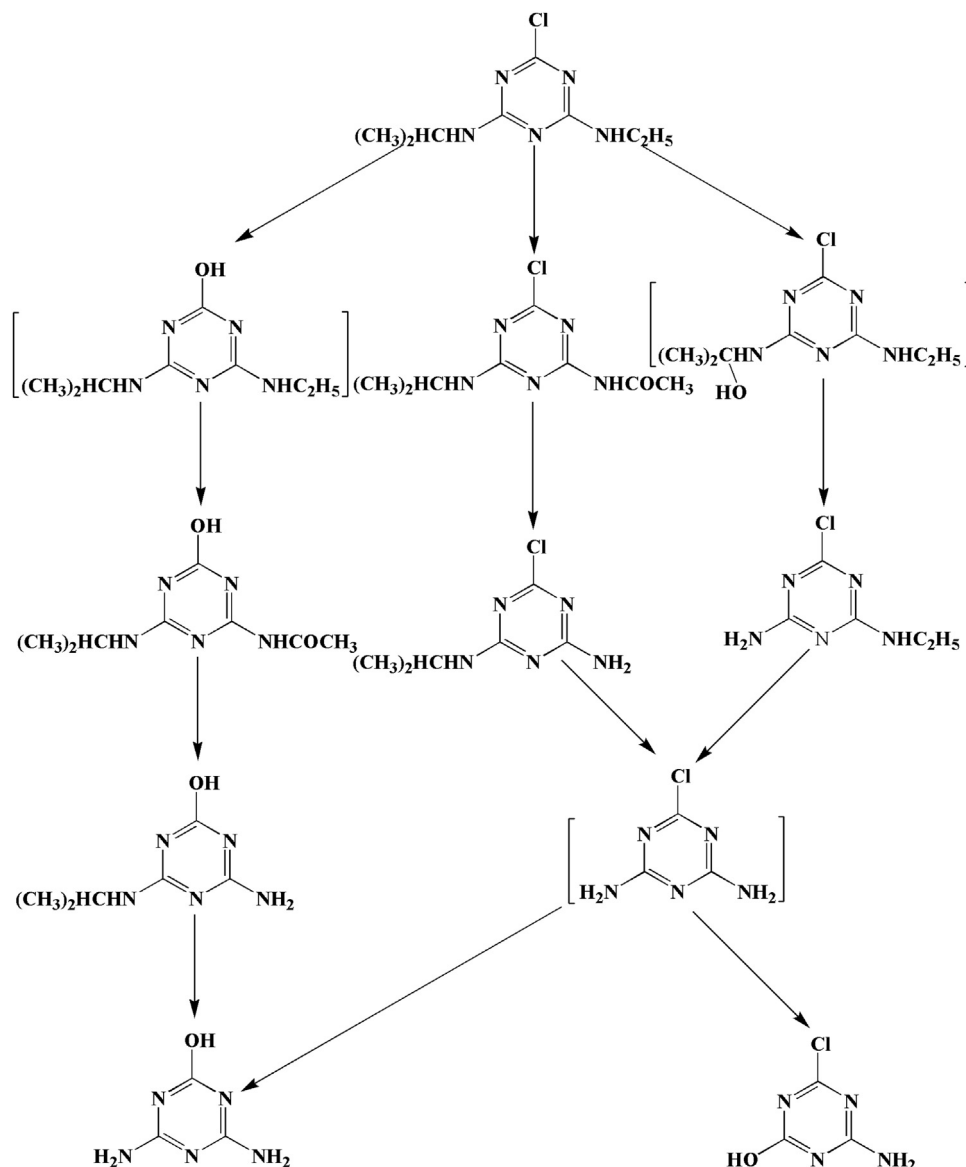


Fig. 6. Photocatalytic degradation (a) and pseudo-first-order kinetic constants (b) of atrazine over all the TiO<sub>2</sub> (A/R) samples under UV-vis light irradiation, (c) HPLC chromatograms during photocatalytic degradation of atrazine with the B-doped TiO<sub>2</sub> (A/R) sample (B5). (d) Time dependence of the fluorescence intensity at 426 nm with all B-doped TiO<sub>2</sub> (A/R). (e) Time dependence of the fluorescence intensity at 426 nm with all B-doped TiO<sub>2</sub> (A/R). (f) Time dependence of the fluorescence intensity at 426 nm with all B-doped TiO<sub>2</sub> (A/R).



**Fig. 7.** Proposed mechanism for photocatalytic decomposition of atrazine by B-doped  $\text{TiO}_2$  (A/R) under UV–vis light irradiation. Compounds I, III, V–VIII, X and XI were experimentally detected.

In the photocatalytic reaction,  $\text{TiO}_2$  absorbs light to produce electron-hole pairs, which migrate to catalyst surface to react with absorbed  $\text{O}_2$  and  $\text{H}_2\text{O}$ , to produce strong oxidizing agents in the form of  $\cdot\text{OH}$  radicals.  $\cdot\text{OH}$  radicals are the main species responsible for the degradation of organic pollutants. The results shown in Fig. 6d clearly show that the generated holes in the newly formed valence bands caused by B-doping could be readily transferred to the surface adsorbed water and hydroxyl groups of the doped  $\text{TiO}_2$  to generate  $\cdot\text{OH}$  radicals. The good linear relationship between fluorescence intensity and irradiation time indicates the stability of the homogeneous B-doped  $\text{TiO}_2$ . In addition to the dominant route of holes attacking water or hydroxyl groups, there was possible another route to produce hydroxyl radicals by the subsequent reactions.

LC/MS analysis was further used to monitor the degradation intermediates to explore the photocatalytic degradation pathways of atrazine by B-doped  $\text{TiO}_2$  (A/R). With our experimental results and literature reports [29–31], the various degradation pathways of atrazine by B-doped  $\text{TiO}_2$  (A/R) are proposed (Fig. 7) and described below:

2-Hydroxyatrazine, 2-chloro-4-ethylamino-6-(1-methyl-1-ethanol)amino-1,3,5-triazine, and desethyl-desisopropyl atrazine could not be found in the LC/MS analysis because of their lower concentration or unstability.

Ammeline (3.70 min), 2-hydroxydesethyl atrazine (4.36 min), 2-chloro-4-amino-6-hydroxy-1,3,5-triazine (4.61 min), 2-hydroxy-4-acetamido-6-amino-1,3,5-triazine (5.15 min), 2,4-diamino-6-chloro-*N*-ethyl-1,3,5-triazine (6.09 min), 2,4-diamino-6-chloro-*N*-(1-methylethyl)-1,3,5-triazine (8.70 min), 2-chloro-4-acetamido-6-isopropylamino-1,3,5-triazine (13.53 min), and atrazine (26.88 min) were detected in the LC–MS analysis (Table 2). These results are in good agreement with those reported previously [29,30].

#### 3.4. Photocatalytic atrazine degradation mechanisms by $\text{TiO}_2$ (A/R) nanocomposites

Three reasons might be mainly responsible for the improved photocatalytic efficiency of the optimal B-doped  $\text{TiO}_2$  (A/R)-B5. Firstly, the phase-junction formed between the anatase

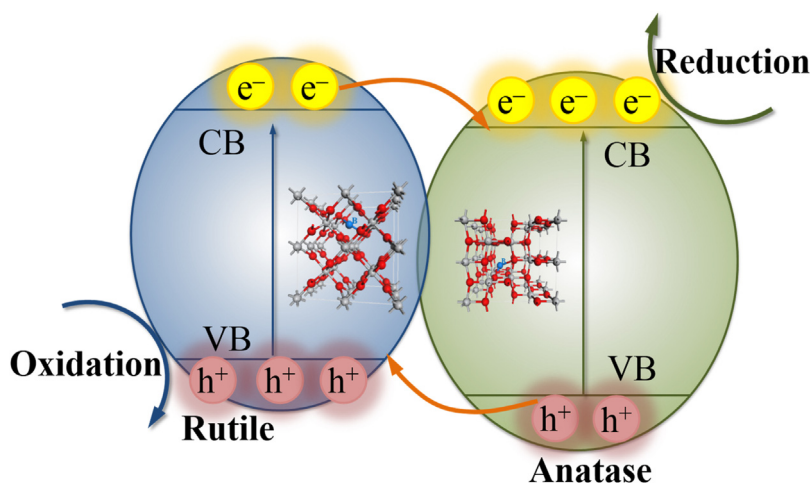


Fig. 8. A proposed valence and conduction band alignment mechanism for the B-doped anatase/rutile interface.

Table 2

The intermediates and their retention time in the photocatalytic degradation of atrazine by B-doped TiO<sub>2</sub> (A/R).

Number	Abbr.	Compounds	Detection time (min)
I	ATRAZINE	Atrazine	26.88
II	OHA	2-Hydroxyatrazine	undetected
III	AOHE	2-Chloro-4-acetamido-6-isopropylamino-1,3,5-triazine	13.53
IV	AOHI1	2-Chloro-4-ethylamino-6-(1-methyl-1-ethanol) amino-1,3,5-triazine	undetected
V	OHOE	2-Hydroxy-4-acetamido-6-isopropylamino-1,3,5-triazine	5.15
VI	DEA	Desethylatrazine	8.70
VII	DIA	Deisopropylatrazine	6.09
VIII	OHDEA	2-Hydroxydesethyl atrazine	4.36
IX	DAA	Desethyldeisopropyl atrazine	undetected
X	AME	2-Hydroxy-4,6-diamino-1,3,5-triazine	3.70
XI	CIOHNH <sub>2</sub>	2-Chloro-4-amino-6-hydroxy-1,3,5-triazine	4.61

nanoparticles and rutile nanoparticles could greatly enhance the photocatalytic activity for photocatalytic activity [32,33]. The presence of phase-junction is beneficial for the separation of photoinduced charge-carriers (pairs of  $e^-$  and  $h^+$ ) and is responsible for the high photocatalytic activity [32]. It is well known that photocatalysis over TiO<sub>2</sub> (or other semiconductors) is usually considered to be initiated upon absorbing a photon whose energy is greater than the band gap energy and generating photoexcited electron-hole pairs. This band alignment, as shown in Fig. 8, could favor the transfer of photogenerated electrons from rutile to anatase, and the transfer of holes from anatase to rutile at a clean interface [34].

Secondly, the capture position of the carriers also increases with the increasing content of dopant B. Such an increase extends the life of the photogenerated carriers, and favors the photogenerated electron-hole separation. Moreover, the surface B favors the electron-hole pairs with the adsorbed water to generate  $\bullet$ OH radicals in the photocatalytic process.

Compared with the non-doped TiO<sub>2</sub>, the B-doped TiO<sub>2</sub> (A/R) can greatly increase the photocatalytic oxidation activity of TiO<sub>2</sub> by shifting valence band to positive, which favors the  $\bullet$ OH radical formation [35,36]. It is well known that the presence of surface hydroxyl groups is advantageous to photocatalytic activity because of their ability to mediate oxidative electron transfer. After the irradiation, the conduction band produces a photoinduced electron, while the interstitial B acts as shallow traps for electrons to prolong the life of the photoinduced charge-carriers (pairs of  $e^-$  and  $h^+$ ), as illustrated by Process II in Fig. 7. This process is essential to improve the UV-vis light catalytic activity of the B-doped TiO<sub>2</sub>.

Finally, the pairs of  $e^-$  and  $h^+$  may diffuse to the surface of the photocatalyst and continue to react with the hydroxyl groups, adsorbed water and oxygen, forming highly active oxidant  $\bullet$ OH. Meanwhile, the surface boron species might also introduce Brønsted and Lewis acid centers onto the surfaces of the B-doped TiO<sub>2</sub> [23]. This also is beneficial to improving the photocatalytic activity of TiO<sub>2</sub>.

All the above reasons enable the B-doped TiO<sub>2</sub> to be an efficient photocatalyst. Thus, B-doping not only tunes the rutile content of the mixed-phase TiO<sub>2</sub>, but also the doping itself enhances the photocatalytic activity.

#### 4. Conclusions

By using a one-step calcination method below phase transition temperature with as-prepared Ti and B mixture as a precursor, B-doped TiO<sub>2</sub> with a tunable rutile/anatase ratio of is successfully synthesized. Both doping and tunable rutile/anatase ratio are responsible for better charge separation via acting as trapping site and phase-junction. The designed and as-synthesized B-doped TiO<sub>2</sub> (rutile/anatase) exhibits a favorable phase-junction structure and a superior photocatalytic activity for the degradation of atrazine under UV-visible light irradiation with 4 times higher rate than the non-doped TiO<sub>2</sub>. This work provides a promising approach to prepare doped TiO<sub>2</sub> with a tunable rutile/anatase ratio for other element doping. Our findings also imply promising applications for the TiO<sub>2</sub> (rutile/anatase) photocatalyst in water and wastewater treatment and are useful to apply this catalyst for the degradation of diverse refractory pollutants under UV-visible light irradiation.

## Acknowledgements

The authors thank the National Science Foundation of China (21590812 and 51538011), the Program for Changjiang Scholars and Innovative Research Team in University and the Collaborative Innovation Center of Suzhou Nano Science and Technology of the Ministry of Education of China for supporting this work.

## References

- [1] E.A. Pappas, C. Huang, *Environ. Sci. Technol.* 42 (2008) 7064–7068.
- [2] L.P. Wackett, M.J. Sadowsky, B. Martinez, N. Shapir, *Appl. Microbiol. Biotechnol.* 58 (2002) 39–45.
- [3] E. Silva, A.M. Fialho, I. Sa-Correia, R.G. Burns, L.J. Shaw, *Environ. Sci. Technol.* 38 (2004) 632–637.
- [4] X. Chen, X.M. Hu, L. An, N.L. Zhang, D.G. Xia, X. Zuo, X.Y. Wang, *Electrocatalysis* 5 (2014) 68–74.
- [5] A. Ventura, G. Jacquet, A. Bermond, V. Camel, *Water Res.* 36 (2002) 3517–3522.
- [6] G.R.P. Malpass, D.W. Miwa, S.A.S. Machado, P. Olivi, A.J. Motheo, *J. Hazard. Mater.* 137 (2006) 565–572.
- [7] H.Z. Chen, S.G. Yang, K. Yu, Y.M. Ju, C. Sun, *J. Phys. Chem. A* 115 (2011) 3034–3041.
- [8] Z.Q. Gao, S.G. Yang, T. Na, C. Sun, *J. Hazard. Mater.* 145 (2007) 424–430.
- [9] R. Jaiswal, N. Patel, A. Dashora, R. Fernandes, M. Yadav, R. Edla, R.S. Varma, D.C. Kothari, B.L. Ahuja, A. Miotello, *Appl. Catal. B Environ.* 183 (2016) 242–253.
- [10] N. Patel, R. Jaiswal, T. Warang, G. Scarduelli, A. Dashora, B.L. Ahuja, D.C. Kothari, A. Miotello, *Appl. Catal. B Environ.* 150 (2014) 74–81.
- [11] Y. Su, S. Han, X. Zhang, X. Chen, L. Lei, *Mater. Chem. Phys.* 110 (2008) 239–246.
- [12] W. Zhao, W.H. Ma, C.C. Chen, J.C. Zhao, Z.G. Shuai, *J. Am. Chem. Soc.* 126 (2004) 4782–4783.
- [13] J. Liu, X. Yu, Q. Liu, R. Liu, X. Shang, S. Zhang, W. Li, W. Zheng, G. Zhang, H. Cao, Z. Gu, *Appl. Catal. B Environ.* 158–159 (2014) 296–300.
- [14] W.K. Wang, J.J. Chen, X. Zhang, Y.X. Huang, W.W. Li, H.Q. Yu, *Sci. Rep.* 6 (2016) 20491.
- [15] G.H. Li, K.A. Gray, *Chem. Mater.* 19 (2007) 1143–1146.
- [16] M. Zúkalova, A. Zúkal, L. Kavan, M.K. Nazeeruddin, P. Liska, M. Gratzel, *Nano Lett.* 5 (2005) 1789–1792.
- [17] S.L. Chen, A.J. Wang, C.T. Hu, C. Dai, J.B. Benziger, *AlChE J.* 58 (2012) 568–572.
- [18] W.K. Wang, J.J. Chen, W.W. Li, D.N. Pei, X. Zhang, H.Q. Yu, *ACS Appl. Mater. Interfaces* 7 (2015) 20349–20359.
- [19] G. Liu, L.Z. Wang, C.H. Sun, X.X. Yan, X.W. Wang, Z.G. Chen, S.C. Smith, H.M. Cheng, G.Q. Lu, *Chem. Mater.* 21 (2009) 1266–1274.
- [20] G.H. Li, C.P. Richter, R.L. Milot, L. Cai, C.A. Schmittenmaier, R.H. Crabtree, G.W. Brudvig, V.S. Batista, *Dalton Trans.* (2009) 10078–10085.
- [21] W.J. Zheng, X.D. Liu, Z.Y. Yan, L.J. Zhu, *ACS Nano* 3 (2009) 115–122.
- [22] G. Liu, X.X. Yan, Z.G. Chen, X.W. Wang, L.Z. Wang, G.Q. Lu, H.M. Cheng, *J. Mater. Chem.* 19 (2009) 6590–6596.
- [23] N.D. Feng, A.M. Zheng, Q.A. Wang, P.P. Ren, X.Z. Gao, S.B. Liu, Z.R. Shen, T.H. Chen, F. Deng, *J. Phys. Chem. C* 115 (2011) 2709–2719.
- [24] D. Chen, D. Yang, Q. Wang, Z.Y. Jiang, *Ind. Eng. Chem. Res.* 45 (2006) 4110–4116.
- [25] K. Yang, Y. Dai, B.B. Huang, *Phys. Rev. B* 76 (2007).
- [26] H. Jin, Y. Dai, W. Wei, B. Huang, *J. Phys. D Appl. Phys.* 41 (2008).
- [27] N. Lu, H. Zhao, J. Li, X. Quan, S. Chen, *Sep. Purif. Technol.* 62 (2008) 668–673.
- [28] T.C. An, X.H. Zhu, Y. Xiong, *Chemosphere* 46 (2002) 897–903.
- [29] V. Hequet, C. Gonzalez, P. Le Cloirec, *Water Res.* 35 (2001) 4253–4260.
- [30] M. Lackhoff, R. Niessner, *Environ. Sci. Technol.* 36 (2002) 5342–5347.
- [31] B. Balci, N. Oturan, R. Cherrier, M.A. Oturan, *Water Res.* 43 (2009) 1924–1934.
- [32] J. Zhang, Q. Xu, Z. Feng, M. Li, C. Li, *Angew. Chem. Int. Ed.* 47 (2008) 1766–1769.
- [33] W. Kim, T. Tachikawa, G.H. Moon, T. Majima, W. Choi, *Angew. Chem. Int. Ed.* 53 (2014) 14036–14041.
- [34] D.O. Scanlon, C.W. Dunnill, J. Buckeridge, S.A. Shevlin, A.J. Logsdail, S.M. Woodley, C.R.A. Catlow, M.J. Powell, R.G. Palgrave, I.P. Parkin, G.W. Watson, T.W. Keal, P. Sherwood, A. Walsh, A.A. Sokol, *Nat. Mater.* 12 (2013) 798–801.
- [35] G. Liu, J. Pan, L.C. Yin, J.T.S. Irvine, F. Li, J. Tan, P. Wormald, H.M. Cheng, *Adv. Funct. Mater.* 22 (2012) 3233–3238.
- [36] T.T. Wu, Y.P. Xie, L.C. Yin, G. Liu, H.M. Cheng, *J. Phys. Chem. C* 119 (2015) 84–89.